Available online at www.sciencedirect.com
SCIENCE DIRECT®
Journal of Solid State Chemistry 179 (2006) 2636–2644
JOURNAL OF SOLID STATE CHEMISTRY
www.elsevier.com/locate/jssc

Synthesis and optical characterizations of undoped and rare-earth-doped CaF_2 nanoparticles

A. Bensalah[a,*], M. Mortier[a], G. Patriarche[b], P. Gredin[c], D. Vivien[a]

[a]*Laboratoire de Chimie de la Matière Condensée de Paris, UMR-CNRS 7574, École Nationale Supérieure de Chimie Paris, 11 rue Pierre et Marie Curie, 75321 Paris Cedex 05, France*
[b]*Laboratoire de Photonique et de Nanostructure, UPR20 CNRS, Route de Nozay, 91460 Marcoussis, France*
[c]*Laboratoire de Chimie de la Matière Condensée de Paris, UMR-CNRS 7574, Université Paris 6, 4 place Jussieu tour 54, 75252 Paris Cedex 05, France*

Received 13 February 2006; received in revised form 18 April 2006; accepted 12 May 2006
Available online 20 May 2006

Abstract

The synthesis of undoped as well as Yb or Er-doped CaF_2 nanocrystals using a reverse micelle method is reported. X-ray powder diffraction and transmission electron microscopy analysis showed that the products were single phased and rather monodispersed with an average particles size around 20 nm. The emission spectra and fluorescence decay times of both Yb^{3+} and Er^{3+} rare earths (RE) ions in CaF_2 nanoparticles are presented. The particles size is increased by heating the as-obtained nanoparticles at different temperatures. The effect of annealing on the optical properties of the two RE ions in CaF_2 is also investigated.

Keywords: Nanoparticles; Reverse micelles; CaF_2; Rare earths; Luminescence

1. Introduction

Over the last decade, nanometer-sized particles have attracted great interest and have become a research focus in terms of both their fundamental and technological importance [1]. Indeed, their physical and chemical properties vary drastically with the size: at nanometer-size, crystallites are influenced by the presence of significant numbers of surface atoms and by the quantum confinement of the electronic states providing novel properties to the nanoparticles compared with their corresponding bulk phases. This is particularly true in the case of luminescent materials since emission lifetime, luminescence quantum efficiency and concentration quenching were found to strongly depend on the particle-size in the nanometer range [2–4]. High efficiencies [3], ultra-fast recombination times [5], interesting nonlinear optical behaviors [6] and unusual fluorescence were observed as well in nanometer-sized crystals [7].

Many nanoparticles of different chemical compositions, shapes and size distributions have been prepared by different kind of methods such as chemical vapor deposition, gas-phase condensation methods, sol–gel processes, micro-emulsion techniques, hydrothermal methods and laser ablation. These methods have been widely investigated first for the production of luminescent semiconductor nanoparticles [8,9]. Lately, considerable effort has been made in the synthesis and the optical spectroscopy of rare earth (RE) doped nano-oxides [10–14]. Investigating and understanding these materials are not only of academic interest but also of technological importance because of their potential applications including advanced phosphor, photonic, display monitors, imaging, light amplification, biological and anti-fraud labeling as well as precursors for transparent ceramics processing.

Fluoride compounds are also very attractive materials for these applications. Compared to oxide-based matrices, they present additional advantages such as a high transparency in a wide wavelength region from the VUV to the IR and a low phonon energy that decreases the non-radiative transition probability of the active ions. However,

*Corresponding author.
E-mail address: amina-bensalah@enscp.fr (A. Bensalah).

0022-4596/$ - see front matter © 2006 Published by Elsevier Inc.
doi:10.1016/j.jssc.2006.05.011

rather few works have been done on RE-doped nanofluorides because of their more delicate chemistry.

Among the fluoride compounds, CaF_2 is an attractive material because of its stability and non-hygroscopic behavior. Besides, recently CaF_2 gained a renewed interest as a laser material when doped with RE ions. In the case of CaF_2:Yb single crystal for instance, thanks to its broad emission bands, very good performances as tunable laser and as ultra-short pulse laser generator were demonstrated [15,16].

Since Boutonnet et al. [17] reported the synthesis of monodispersed metallic particles, micro-emulsions have been successfully used for the synthesis of several undoped and RE-doped compounds [18]. These micro-emulsions consist in fact of reverse micelles resulting from the thermodynamically stable organization of surfactant which encapsulate a nanosized water core in contact with their hydrophilic head groups. The hydrophobic tails of the surfactant are solvated by the solvent. When water-soluble polar and ionic substances are dissolved within the water core, the solvent is left essentially unaltered. As a result, reactions involving the dissolved substances occur directly inside the micelle cores.

In this context, we investigated the synthesis of CaF_2 nanocrystals undoped and doped with Yb^{3+} or Er^{3+}, as luminescent ions, by using the Igepal®/cyclohexane/water reverse micelles system. The obtained nanoparticles are characterized and fluorescence measurements are performed to determine the optical characteristics of CaF_2:Yb and CaF_2:Er nanocrystals. The effect of annealing, at different temperatures, on the fluorescence spectra and fluorescence decay times is also investigated.

2. Experimental

2.1. Nanoparticles synthesis

All syntheses were made using commercially available products. Hydrated calcium and RE nitrates (99.99%), as well as Igepal CO-520 (polyoxoethylene nonyl phenol) were from Aldrich. In all, 40 wt% aqueous HF, absolute ethanol (99.99%) and cyclohexane (99%) were also used. Water was distilled. There was no further purification of any of the chemicals used in this study.

Following Kumar et al. [19], Bender et al. [20] used the reverse micelles system to synthesize BaF_2 nanoparticles. We adapted this method for the synthesis of undoped and RE-doped CaF_2 nanoparticles. Since $(Ca(NO_3)_2)$ has a higher solubility limit in water than $(Ba(NO_3)_2)$, a higher amount of CaF_2 can be obtained in one experiment. Microemulsions were made by dissolving 15 g of Igepal in 50 mL of cyclohexane inside a 100 mL teflon beaker. This mixture was stirred magnetically until it was homogeneous and then 10 mL of a 0.3 mol/L $Ca(NO_3)_2$ aqueous solution was poured-in slowly and the microemulsion was stirred for a short time. Since a rather large domain of CaF_2 solid solution exists in the CaF_2–REF_3 system, up to 30% of YbF_3 in the case of CaF_2–YbF_3 phase diagramme [21], we chose to test the synthesis of CaF_2:RE with a relatively high RE concentration (10 mol%) and check whether it is possible or not to incorporate this doping amount in the CaF_2 nanoparticles. For this purpose, 0.03 mol/L of $RE(NO_3)_3$ where added to the preceding calcium nitrate solution. Finally, 5 mL of EtOH, as a co-surfactant [20], was added to the solution. In a similar way, a hydrofluoric acid microemulsion was made by substituting the aqueous calcium nitrate solution with a 10 mL aqueous HF solution at 0.625 mol/L. These two microemulsions were then mixed and stirred at room temperature (RT), for 2 h, in order to allow the inter-micellar exchange to proceed, leading to the formation of pure or doped CaF_2 nanoparticles according to the reaction:

$$(1-x)Ca(NO_3)_2 + xRE(NO_3)_3 + (2+x)HF \rightarrow (Ca_{(1-x)}RE_x)F_{2+x}\searrow + (2+x)HNO_3, \quad (1)$$

in which $x = 0$ or 0.1

The emulsion mixture was centrifuged at 13,000 rpm for 20–60 min, which caused sedimentation of the nanoparticles and allowed the removal of the mother liquor. The particles were then washed and centrifuged with ethanol and cyclohexane alternatively, several times. Finally the product was oven dried at 120 °C and lightly crushed in an agate mortar.

In order to investigate the annealing effect, we heated the obtained nanoparticles at different temperatures, between 200 and 800 °C, under argon atmosphere for 4 h. The furnace was vacuumed before argon treatment.

2.2. Measurements

Powder X-ray diffraction (XRD) measurements were performed on a Siemens D5000 mounted in a Bragg Brentano configuration using a Fe-filtered Co-radiation diffraction ($\lambda_{K\alpha1} = 1.789$ Å $- \lambda_{K\alpha2} = 1.793$ Å). The 2θ angular resolution was 0.05°. The diffraction patterns were scanned over the 2θ range 20–80°. The nanoparticles size L was evaluated by using the Scherrer formula:

$$L = \frac{\lambda}{\Delta(2\theta) \times \cos\theta},$$

where λ is the diffractometer wavelength, 2θ the peak position and $\Delta(2\theta)$ the peak-width at half-maximum, corrected from the instrumental broadening. The lattice cell parameter a of the crystalline phase was deduced from the Bragg peaks angular positions.

Transmission electron microscopy (TEM) was performed on a 200-kV Phillips CM20 microscope. The fine powder sample was placed onto a carbon-coated copper grid. TEM images and the associated selected area electron diffraction (SAED) patterns were studied, allowing the evaluation of the fluoride nanocrystals size and the interplanar spacing d. High resolution TEM (HRTEM) images were taken to observe atomic planes inside the nanocrystals. The microscope was equipped with an energy

dispersive X-ray (EDX) analyzer which enabled calcium fluoride nanocrystals microanalysis.

Infrared (IR) spectra were obtained from anhydrous KBr pellet using a FTIR spectrometer and were referenced against a freshly prepared blank KBr pellet.

Emission spectra in the visible were recorded under 8-ns pulsed excitation using a tunable optical parametric oscillator (OPO), pumped by the third harmonic of a Q-switched Nd^{3+}:YAG laser (355 nm). The fluorescence was analyzed through a 250-mm monochromator equipped with an optical multichannel analyzer. Emission spectra in the infrared range were recorded under a CW excitation with a titanium-sapphire laser, pumped by an argon ion laser. The fluorescence was analyzed through a 750 mm double monochromator and then detected by a liquid nitrogen cooled Ge-cell.

Fluorescence decay profiles in the infrared range and in the visible range were obtained under pulsed excitation using the OPO. The infrared fluorescence was detected by an InAs cell cooled at 77 K and connected to an oscilloscope. Appropriate band-pass filters were used to select the wavelength of interest. The time-resolved visible fluorescence was analyzed with a 250-nm monochromator and detected by the optical multichannel analyzer. All the PL measurements were done under constant excitation laser intensity of 200 mW and under the same geometrical conditions in order to avoid macroscopic reabsorption effects (radiative trapping) that could result in some modification in the shape and intensity of the emission spectra and artificial lengthening of the decay times.

3. Results and discussion

3.1. Synthesis

For the sake of comparison, we considered first the synthesis of undoped CaF_2 nanoparticles by direct precipitation route. In this case, the synthesis procedure consists of dissolving $Ca(NO_3)_2$ in an aqueous HF solution. After stirring, centrifugation, washing and drying, the precipitate was identified as cubic CaF_2 by XRD measurement. The TEM micrographs revealed that the obtained powder consists mainly of large aggregates, about 500 nm, composed of irregular shaped particles with a size of around 20 nm (Fig. 1). This synthesis process will not be further considered in this paper.

In order to get better-separated particles, we investigated another soft chemistry route consisting of the reverse micelles method as described above. The product is obtained by the reaction of Ca^{2+} and F^- ions for the undoped particles and of Ca^{2+}, RE^{3+} and F^- in the case of RE-doped particles in a reverse micellar system.

FTIR absorption was measured in order to check the purity of the obtained washed powder. The spectrum recorded from 400 to 4000 cm^{-1}, presented in Fig. 2, shows strong absorption bands at 3400 and 1600 cm^{-1} characteristic of anti-symmetric and symmetric stretches, and

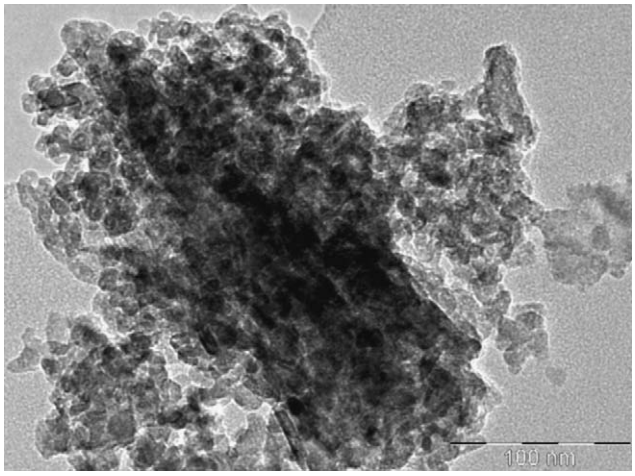

Fig. 1. TEM image of CaF_2 nanoparticles obtained by direct precipitation of $Ca(NO_3)_2$ in an HF solution. The obtained powder consists mainly of large aggregates.

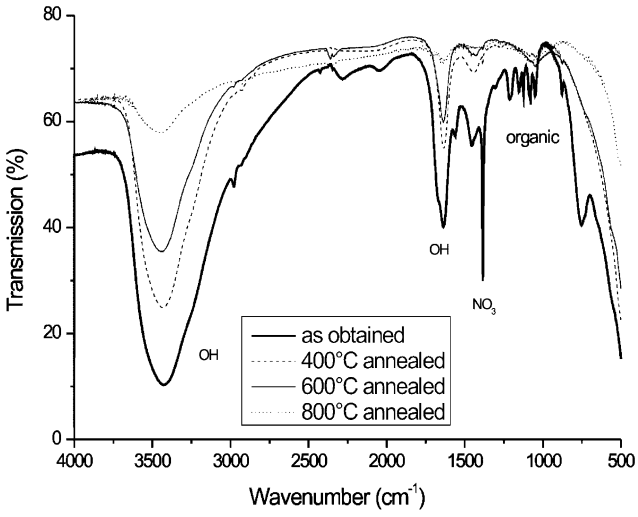

Fig. 2. FTIR spectra of CaF_2 nanoparticles as obtained and annealed at different temperatures.

bending modes of the H_2O molecule, respectively revealing the presence of water (or hydroxyl groups) in the as-obtained powder. Furthermore, a band at 1385 cm^{-1} that can be attributed to the asymmetric stretching vibration of NO_3^- was clearly seen in the IR spectra, as nitrate salts were used in the synthesis. Residual organics are also detected on the spectrum of the as synthesized powder around 1100 cm^{-1}. After additional washing in water and ethanol, the amount of nitrate and organic could be decreased. Besides, as can be seen in Fig. 2, the FTIR spectra recorded on the synthesized powder after annealing at different temperatures are also presented. After annealing at 400 °C, the traces of organics are removed and the nitrates are strongly decreased. With increasing the annealing temperature from 400 to 600 °C the nitrates are not detectable any more. The intensity of the strong absorption bands related to the presence of water or hydroxyl groups in the as-obtained powder decrease continuously with the annealing

temperature revealing a loss in the amount of these molecules with annealing.

3.2. Undoped CaF_2 nanoparticles from the reverse micellar method

The XRD diagram of the as-obtained calcium fluoride particles is presented in Fig. 3. All the peaks can be indexed in the CaF_2 cubic phase of the fluorite-type structure (space group: *Fm*3*m*) [22].The XRD pattern presents broad peaks revealing the very small crystallite size of the synthesized compound. Peaks position 2θ and width at half-maximum $\Delta(2\theta)$ were deduced from the peaks fitting using Lorentzian line shape. Using the Scherrer equation, the average crystallite size was evaluated at 17.0 ± 0.8 nm, based on the three first diffraction lines. The lattice parameter $a = 5.460 \pm 0.001$ Å, calculated from the obtained XRD diagram, is in good agreement with the literature [22].

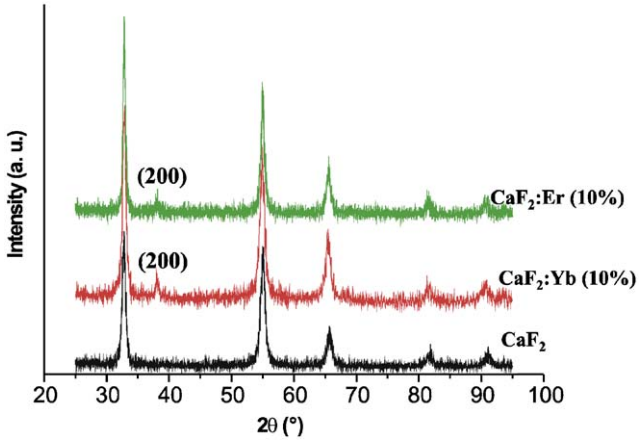

Fig. 3. XRD diagrams of undoped and 10% RE-doped CaF_2 (*Re* = Yb, Er) nanoparticles obtained by the reverse micelles method.

The as-obtained powder was analyzed by TEM. Fig. 4(a) represents the bright field micrograph of the undoped CaF_2 nanoparticles, with the associated SAED in the insert. Because of the presence of many crystallites in diffraction conditions, like in a polycrystalline material, virtual circles are observed on the diffraction pattern. The analysis of the SAED pattern gives the inter-planar spacing *d* which enable to index the spots and to calculate the unit cell parameter $a = 5.450 \pm 0.014$ Å. This value is close to that measured from the XRD diagram, showing a good agreement between these two independent measurements.

On the TEM image at a higher magnification (Fig. 4(b)), we can observe dispersed nanoparticles with cubic shapes reflecting the cubic structure of CaF_2. Comparing with the powder obtained by direct precipitation (Fig. 1), the nanoparticles synthesized by the reverse micelles method are better dispersed and no aggregates are observed in this case.

The particles size distribution, obtained from the analysis of the TEM image (Fig. 4(b)) is presented in Fig. 4(c). It shows an average particle size of 20 nm with a standard deviation of 5 nm. Sun et al. [23] obtained similar CaF_2 nanocubes using a direct precipitation route followed by a hydrothermal treatment but their particles were of a larger size, around 300 nm.

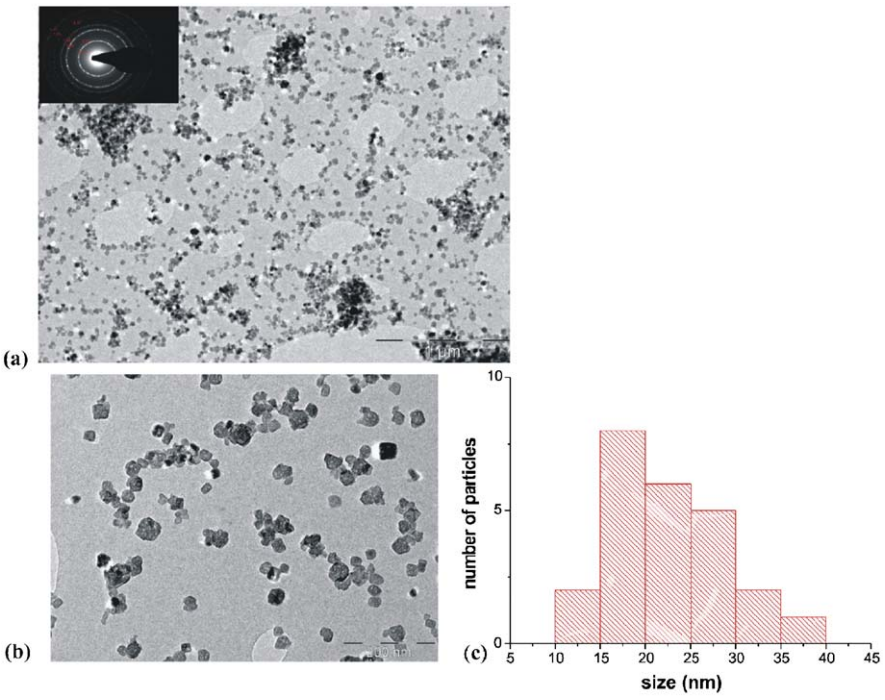

Fig. 4. (a) TEM image of the undoped CaF_2 nanoparticles obtained by the reverse micelles method and the corresponding SAED pattern, (b) higher magnification of the as-obtained undoped CaF_2 nanoparticles and (c) the corresponding particles size distribution.

Energy dispersive X-ray microanalysis (EDX) were made on several particles and reveals a homogeneous chemical composition for the undoped CaF_2 nanoparticles. Oxygen traces were detected in the obtained powder. However, since oxygen was detected only when the electron beam was focused on isolated particles, it reveals that the oxygen is probably adsorbed at their surface.

3.3. RE-doped CaF_2 nanoparticles from the reverse micellar method

The XRD diagrams of the as-obtained RE-doped CaF_2 particles, shown in Fig. 3, present similar broad peaks as for the undoped CaF_2 revealing comparable particles size. Indeed, the average size of the RE-doped CaF_2 particles, calculated with the Scherrer formula, is about 18.0 ± 0.7 nm.

For undoped CaF_2, the (200) peak corresponds to an allowed X-ray diffraction of the fluorite-type structure but with a negligible intensity (Fig. 3). When doping with 10% of Yb^{3+} or Er^{3+}, which substitutes the Ca^{2+} site, the intensity of the (200) diffraction peak increases because of the difference in the atomic number Z between the RE and the calcium elements, especially at high doping level. Indeed, as reported in the literature, [24], the (200) peak appears clearly for the $Ca_{0.8}Yb_{0.2}F_{2.2}$ composition of the CaF_2–YbF_3 solid solution. The appearance of this peak in the XRD diagram of the RE-doped CaF_2 is a signature of the RE incorporation in the CaF_2 host. The reverse micellar method allows thus the synthesis of $Ca_{0.9}RE_{0.1}F_{2.1}$ nanoparticles. The lattice parameter calculated from the XRD pattern of the RE-doped CaF_2 nanoparticles is $a = 5.480 \pm 0.001$ Å. This value is in agreement with the observation in high resolution (HR-TEM) which exhibits well defined (111) planes in many nanoparticles. Indeed, the distance d between these planes is estimated at ~3.1 Å.

Though Yb^{3+} or Er^{3+}, in 8-fold coordination, have a smaller ionic radius ($r_{Yb} = 1.125$ Å, $r_{Er} = 1.144$ Å) than Ca^{2+} ($r_{Ca} = 1.26$ Å) [25], the RE-doped CaF_2 has a larger lattice parameter ($a = 5.48$ Å) than the undoped compound ($a = 5.46$ Å). In fact, when Ca^{2+} is substituted by a trivalent RE ion, charge balance compensating F^- ions enter the fluorite structure in interstitial fluoride cubic sites and the electronic repulsion between F^- ions leads to a net increase of the lattice parameter.

In the case of RE-doped CaF_2, the obtained nanoparticles morphology is rather irregular. An example of Yb-doped CaF_2 is shown in Fig. 5(a). This difference, with regard the undoped CaF_2, is certainly due to the F^- ions interstitials which lead to a dominant defect structure [26,27], especially at high doping levels. Moreover, the defects in the RE-doped CaF_2 can aggregate and form clusters [28] which should have an effect on both speed and orientation of the particles growth. The obtained RE-doped CaF_2 nanoparticles morphology should be then affected and differ from the undoped CaF_2 nanoparticles obtained by the same method. The particles size distributions for CaF_2:Yb nanoparticles is presented in Fig. 5(b). The calculated average particles size is 19 nm, with a standard deviation of 5 nm, shows a good agreement with the particles size measured from the XRD diagram. Similar results are obtained for CaF_2:Er.

The chemical composition of the doped nanoparticles is homogeneous and the average RE-dopant concentration measured by EDX on several single particles is equal to the one in the starting solution (10%) which confirms a good incorporation of the RE in the CaF_2 nanoparticles.

The obtained RE-doped CaF_2 nanoparticles were heated during 4 h at different temperatures under Argon. X-ray diffraction diagrams were recorded for the different CaF_2:Yb samples heated from 200 to 800 °C. Up to 400 °C the X-ray patterns are similar with relatively broad peaks. From 600 °C, we can clearly see the narrowing of the X-ray diffraction peaks revealing the growth of the powder particles. Indeed, the particles size estimated from the Scherrer equation increases from ~20 nm, for the as prepared nanocrystals, to more than 500 nm after heating at 800 °C.

These results are confirmed by the TEM images. Annealing the as-obtained nanoparticles up to 400 °C allows, as mentioned before, the loss of the residual organic and NO_3^- traces without increasing the size of the

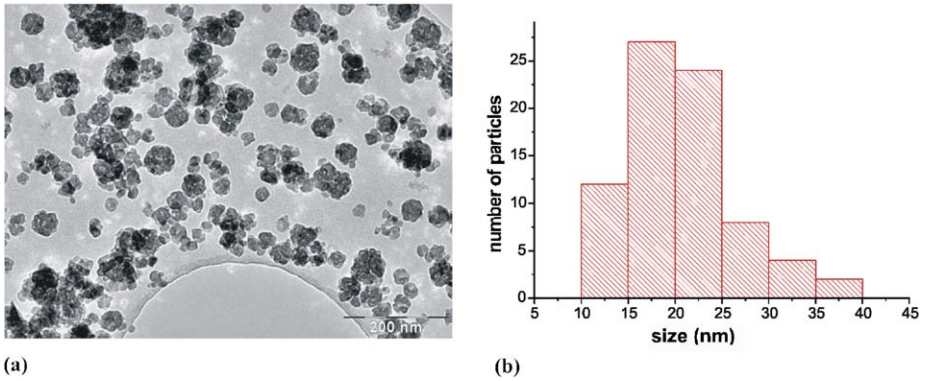

(a) (b)

Fig. 5. (a) TEM image of the CaF_2:Yb^{3+} (10%) nanoparticles obtained by the reverse micelles method and (b) the corresponding particles size distribution.

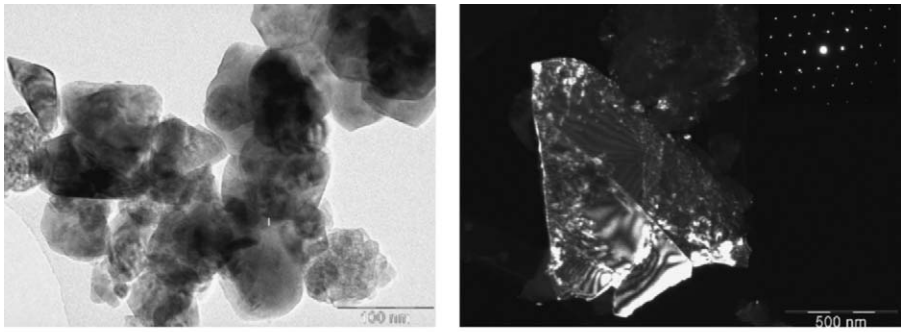

Fig. 6. TEM image of the CaF_2:Yb^{3+} (10%) nanoparticles obtained by the reverse micelles method (a) after annealing at 600 °C and (b) the 1 1 1 dark field image of a single crystal obtained after annealing at 800 °C. In the inset of (b), the electron diffraction pattern proves that the single crystal is in a ⟨110⟩ zone axis orientation.

nanoparticles. At 600 °C, we observe a growth and probable coalescence of the nanoparticles (Fig. 6a) while at 800 °C micron size single crystals are obtained as can be seen on the dark field image of Fig. 6b. In the inset, the associated selected area electron diffraction pattern proves that the heated particles at 800 °C is a cubic phased single crystal oriented along a ⟨110⟩ zone axis. To sum up, the annealing treatment has two effects: removing the adsorbed molecular species and increasing the particles size.

3.4. Optical characterization of re-activated CaF_2 nanocrystals

The fluorescence spectra of the RE-doped CaF_2 nanoparticles, recorded at RT are presented in Fig. 7. In the case of CaF_2:Yb, emission spectra, obtained under 930 nm excitation, present broad bands in the 900–1200 nm region due to different electronic transitions between the $^2F_{5/2}$ excited state down to the various Stark levels of the $^2F_{7/2}$ ground state. Generally, Yb^{3+} presents broader peaks with respect to the other RE ions, especially at RT, due to the large splitting of the $^2F_{7/2}$ ground state, the thermal spreading of the spectrum and the strong electron–phonon coupling which characterize this ion [29]. Besides, the appearance of several crystallographic sites in the case of CaF_2 host when doped with trivalent RE contributes to the broadening of the fluorescence bands [28]. The shape of the emission spectra obtained on Yb-doped CaF_2 nanoparticles is similar to that of Yb^{3+}-doped CaF_2 single crystal [28,30].

However, the fluorescence intensity seems to be dependent on the annealing temperature. Fig. 7(a) shows the emission spectra of Yb-doped CaF_2 nanoparticles as obtained and heated at different temperatures and consequently with different particles size.

A slight increase in the luminescence intensity is observed with the increase of the annealing temperature up to 600 °C while it dramatically increase when the annealing temperature rises from 600 to 800 °C. Indeed, comparing to the emission spectrum recorded for the as-obtained nanopowder, with particles of 20 nm in size, the

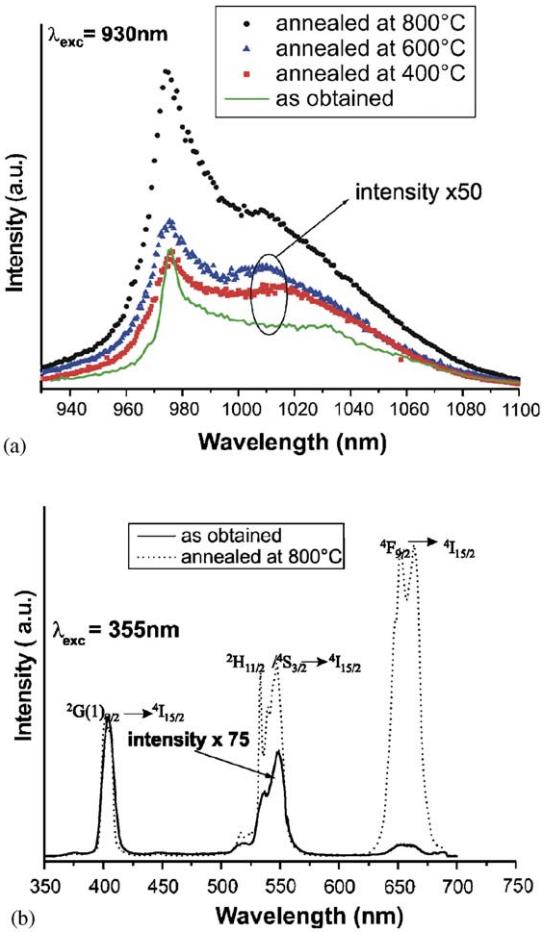

Fig. 7. Emission spectra of (a) CaF_2:Yb nanoparticles as obtained and annealed at different temperatures, under 930 nm excitation and (b) CaF_2:Er nanoparticles as obtained and annealed at 800 °C, under 355 nm excitation. For better comparison, the spectra are normalized on the first peak at 410 nm.

fluorescence intensity increases by a factor 100 for the sample heated at 800 °C, with particles over 500 nm in size. Furthermore, the Yb fluorescence lifetime is 40 μs for the as-obtained samples while it increases to 1.26 ms for the sample annealed at 800 °C. This phenomenon, which has

been observed in other RE-doped materials with nanometric size [31–34], is generally attributed to size and surface effects. It is known that the coordination of the atoms on the surface is different from that in the bulk; atoms on the surface do not have a full coordination sphere which leads to a higher potential energy [8]. Therefore, various chemical species can be easily adsorbed at the surface of the particles. Considering that our synthesis process is achieved with nitrates salt in water and organic solutions, the surface of the nanoparticles can be easily covered by residual organic, NO_3 and OH groups as detected by FTIR spectroscopy. Such groups, with high phonon frequencies, are well known to efficiently quench the luminescence [35] and thus explain the weak emission intensity and short fluorescence lifetime of the as-obtained nanoparticles. Once they are heated up to 800 °C the luminescence efficiency improves and the decay time increases strongly. The enhancement of the luminescence and the lengthening of the decay times, related to the annealing temperature, are ascribed to two main factors: the decrease of the surface quenching centers and the increase of the particles size. These two factors are, nevertheless, somehow related. Indeed, the heating treatment removes the adsorbed species at the surface of the particles through first, their desorption or decomposition during the annealing process and second, through the decrease of the specific surface area associated to the increase of the particles size, leading to a decrease of the quenching centers at the surface of the particles. Besides, another process related to the increase of the particles size which contributes to the enhancement of the luminescence is that the probability for the luminescence to be quenched at the particle surface is all the less since the particle size is big. Indeed, the migration of the energy emitted by a luminescent center to the surface is less probable in a big particle tan in a smaller one as the crossed distance is larger.

Up to 400 °C, as it was proved by DRX and TEM images, the nanoparticles size does not increase. Thus, the slight increase in the luminescence cannot be attributed to a size effect but to the desorption or the decomposition of some of the adsorbed quenching species at the surface of the particles. Moreover, though the residual nitrates and organic traces are removed after annealing at 600 °C, as proved by the FTIR measurements, the luminescence intensity increases slightly what suggests that these species do not play a major role in the quenching mechanism. What mainly quench the luminescence are thus, the OH groups bonded on the particles surface. When the particles are rather small, below 600 °C, if there are a still few hydroxyl groups left on the surface, they will be close enough to quench most of the luminescent ions and therefore the global intensity is still quite small. Above 600 °C the particle size increases strongly and a big amount of luminescent ions are far enough from the surface, and hence from the OH groups, in order not to be quenched. As a direct consequence the luminescence increases greatly.

A similar behavior is observed for the 10% Er-doped CaF_2 nanoparticles. No strong change is noticed in the luminescence spectra recorded for the as-obtained CaF_2:Er nanoparticles and the ones annealed between 200 and 600 °C while, as in the case of Yb-doped CaF_2 nanoparticles, a strong enhancement of the luminescence intensity occurs after annealing at 800 °C. Fig. 7(b) shows typical erbium fluorescence spectra, recorded at RT under ultraviolet excitation (355 nm) for both as-obtained and 800 °C annealed powders. The spectra show several peaks lying from the near UV to the near infrared region, characteristic of the Er^{3+} ion electronic transitions. Indeed, when the $^4G_{9/2}$ level is populated under 355 nm excitation, it relaxes non-radiatively to the different levels below (Fig. 8). This first step is then followed by several radiative transitions toward the $^4I_{15/2}$ ground state, giving rise to the violet, green and red emissions. As in the case of Yb^{3+}, the emission intensity is higher (by a factor ~75) for the CaF_2:Er nanosized powder heated at 800 °C than for the as obtained one.

Moreover, the spectrum of the annealed powder is dominated by the ($^4F_{9/2} \rightarrow {}^4I_{15/2}$) red emission. It is reported that, at low concentration in different compounds, the green emission is dominant because the two $^4S_{3/2}$ and $^2H_{11/2}$ levels decay mostly radiatively to $^4I_{15/2}$ [36–39]. However, at high doping level, different cross-relaxation processes such as ($^4S_{3/2}$, $^4I_{9/2}$)→($^4I_{15/2}$, $^4I_{13/2}$) and ($^4S_{3/2}$, $^4I_{9/2}$)→($^4I_{13/2}$, $^4I_{9/2}$) becomes dominant [36,40] and depopulate the $^4S_{3/2}$ and $^2H_{11/2}$ green emitting levels. As a result, the Er^{3+} green emission is weakened. Besides, another cross-relaxation process ($^4F_{7/2}$, $^4F_{9/2}$)→($^4I_{11/2}$, $^4F_{9/2}$) may contribute to

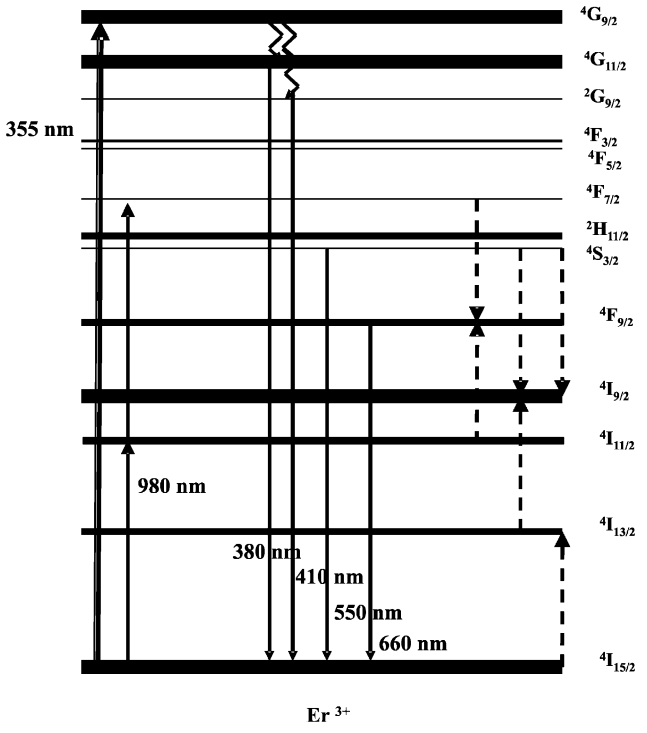

Fig. 8. Energy levels diagram of the Er^{3+} RE ion.

increase the population of the $^4F_{9/2}$ red emitting level [40]. In our sample, the erbium content, 10%, is high. Consequently, the higher intensity of the red emission, compared to the green one, observed for the heated powder (Fig. 7(b)) is due to the above-mentioned cross-relaxation processes enhanced at high erbium concentration.

For the as-obtained CaF_2:Er nanoparticles, with high phonon frequencies groups coordinated at their surface, we observe that the relative intensity of the red to green emissions is weaker though the Er concentration is identical in both, annealed and as-obtained samples. This variation of the red emission intensity, before and after annealing, can be explained by less efficient cross-relaxation processes in the as-obtained nanosized particles due to the presence of high phonon frequency quenching centers. Thus, the depopulation of the $^2H_{11/2}/^4S_{3/2}$ levels as well as the population of the red $^4F_{9/2}$ level, by cross-relaxation processes, are weakened and the green emission is favored.

In all the Er-doped samples, emission at ~1.5 μm corresponding to the $^4I_{13/2} \rightarrow {}^4I_{15/2}$ transition is also observed. The decay time of the $^4I_{13/2}$ level for the annealed sample, under 980 nm excitation, is 11.8 ms while it is shortened to 10 μs for the as-obtained sample. This behavior, again, reflects the role of the annealing which eliminates the quenching centers at the surface of the particles.

This annealing effect is even more obvious in the case of the Er up-conversion emission under near-IR excitation (980 nm). The up-conversion mechanism of Er^{3+} ions are well known [37,38] and consists mainly of excited state absorption (ESA) and energy transfer up-conversion (ETU). The laser excitation at 980 nm induces the transition from the Er^{3+} $^4I_{15/2}$ ground state to the $^4I_{11/2}$ excited state. The second excitation step brings the excited ion from $^4I_{11/2}$ to $^4F_{7/2}$. Then, the $^4F_{7/2}$ level decays non-radiatively to the green emitting $^4S_{3/2}$ and $^4H_{11/2}$ close levels (in thermal equilibrium) as well as to the red emitting $^4F_{9/2}$ level. A third excitation step can bring the Er^{3+} ion to the $^4G_{7/2}$, $^2K_{15/2}$ and $^4G_{9/2}$ excited states giving rise to the violet emissions (Fig. 8).

Fig. 9 presents the room temperature up-conversion spectra for the CaF_2:Er (10%) samples. The heated powder shows very efficient 2-photons red and green up-conversion emissions and weak 3-photons violet fluorescence after near IR excitation (Fig. 9(a)). For the annealed particles the up-conversion emission is dominated by the 2-photons up-conversion red emission as in the case of direct emission under 355 nm excitation (Fig. 7(b)). The three photons up-conversion emission is weak, since it goes as the third power of the excitation power.

In the case of the as-obtained particles, the up conversion emission yield is very weak and only a green emission can be detected (Fig. 9(b)). The up-conversion emission arises from a nonlinear second-order process and so is very sensitive to impurity traces and quenching phenomena. Indeed, in the presence of high phonon frequencies groups, both the $^4I_{11/2}$ intermediate level and the emitting one are depopulated through non-radiative processes, which results in a drastic decrease of the overall up-conversion emission. If an Er^{3+} ion is nevertheless excited by up conversion, the green emission is favored, because the cross-relaxation processes, populating the red emitting level and depopulating the green ones, are less efficient in the presence of quenching centers as mentioned before in the case of direct emission.

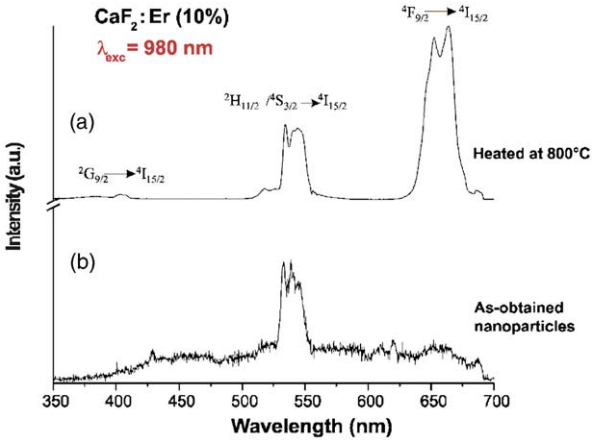

Fig. 9. Up-conversion emission spectra, under 980 nm excitation of (a) CaF_2:Er^{3+} (10%) nanoparticles annealed at 800 °C and (b) of as-obtained CaF_2:Er^{3+} (10%) nanoparticles.

4. Conclusion

In this work, nanoparticles of CaF_2 undoped and doped with Yb or Er, with an average size of about 20 nm, were synthesized by the Igepal/cyclohexane/water reverse micelles method. The XRD, TEM and EDX characterization showed that the obtained nanoparticles are single phased with homogeneous chemical composition. Undoped nanoparticles have a cubic shape while doping with trivalent RE leads to more irregular morphology.

The optical measurements performed on the as-obtained CaF_2:Yb and CaF_2:Er nanoparticles showed a rather low fluorescence efficiency and very short decay times. However, annealing the nanopowders at different temperatures dramatically enhanced the luminescence, by a factor ~100 and lengthened the decay times. This variation is caused by the release of surface species such as water molecules or hydroxyl groups and the increase of the particles size, upon heating leading to a decrease of the non-radiative de-excitation phenomena. Furthermore, the increase of the particles size decreases the energy migration probability towards the surface quenching centers. For the 10% Er-doped CaF_2 particles, annealed at 800 °C, the luminescence spectra are dominated by the red emission due to the cross relaxation processes. The effect of the surface quenching centers is evidenced by the decrease of the red to green emission ratio in the as-obtained sample, compared to the annealed one.

Acknowledgment

This study is supported by the DGA under Grant No. 05 34020.

References

[1] R.P. Andres, R.S. Averback, W.L. Brown, L.E. Brus, W.A. Goddard, A. Kaldor, S.G. Louie, M. Moscovits, P.S. Peercy, S.J. Riley, R.W. Siegel, F. Spaepen, Y. Wang, J. Mater. Res. 4 (1989) 704–736.
[2] S. Sun, C.B. Murray, J. Appl. Phys. 85 (1999) 4325–4330.
[3] C. Suryanarayana, Int. Mater. Rev. 40 (1995) 41–64.
[4] F.E. Kruis, H. Fissan, A. Peled, J. Aerosol Sci. 29 (1998) 511–535.
[5] T. Hase, T. Kano, E. Nakazawa, H. Yamamoto, Adv. Electron. Phys. 79 (1990) 271–373.
[6] G. Wakefield, H.A. Keron, P.J. Dobson, J.L. Hutchison, J. Colloid Interface Sci. 215 (1999) 179–182.
[7] G. Wakefield, H.A. Keron, P.J. Dobson, J.L. Hutchison, J. Phys. Chem. Solids 60 (1999) 503–508.
[8] X. Peng, M.C. Schlamp, A.V. Kadavanich, A.P. Alivisatos, J. Am. Chem. Soc. 119 (1997) 7019–7029;
G. Counio, T. Gacoin, J.P. Boilot, J. Phys. Chem. B 102 (1998) 5257–5260.
[9] T. Trindade, Chem. Mater. Rev. 13 (2001) 3843–3858.
[10] R. Bazzi, M.A. Flores, C. Louis, K. Lebbou, W. Zhang, C. Dujardin, S. Roux, B. Mercier, G. Ledoux, E. Bernstein, P. Perriat, O. Tillement, J. Colloid Interface Sci. 273 (1) (2004) 191–197.
[11] M. Nishi, S. Tanabe, M. Inoue, M. Takahashi, K. Fujita, K. Hirao, Opt. Mater. 27 (2005) 655–662.
[12] A.J. Rulison, R.C. Flagan, J. Am. Ceram. Soc. 77 (12) (1994) 3244–3250.
[13] A. Patra, C.S. Friend, R. Kapoor, P.N. Prasad, Chem. Mater. 15 (2003) 3650–3655.
[14] B. Masenelli, P. Melinon, D. Nicolas, E. Bernstein, B. Prevel, J. Kapsa, O. Boisron, A. Perezl, G. Ledoux, B. Mercier, C. Dujardin, M. Pellarin, M. Broyer, Eur. Phys. J. D 34 (2005) 139–143.
[15] V. Petit, J.L. Doualan, P. Camy, V. Menard, R. Moncorge, Appl. Phys. B 78 (2004) 681–684.
[16] A. Luccas, G. Debourg, M. Jacquemet, F. Druon, F. Balembois, P. Georges, P. Camy, J.L. Doualn, R. Moncorge, Opt. Lett. 29 (23) (2004) 2767–2769.
[17] M. Boutonnet, J. Kizling, P. Stenius, G. Maire, Colloids Surf. 5 (1982) 209–225.
[18] M.P. Pileni, Langmuir 13 (1997) 3266–3276.
[19] P. Kumar, V. Pillai, S.R. Bates, D.O. Shah, Mater. Lett. 16 (1993) 68–74.
[20] C.M. Bender, J.M. Burlitch, Chem. Matter 12 (2000) 1969–1976.
[21] B.P. Sobolev, P.P. Fedorov, J. Less. Common. Met. 60 (1978) 33–46.
[22] L. Gerward, J.S. Olsen, S. Streenstrup, M. Malinowski, S. Asbrink, A. Waskowska, J. Appl. Crystallogr. 25 (1992) 578–581.
[23] X. Sun, Y. Li, Chem. Commun. 14 (2003) 1768–1769.
[24] N.B. Grigoreva, L.P. Otroshchenko, B.A. Maksimov, I.A. Berin, B.P. Sobolev, V.I. Simonov, Kristallografiya, 1996 Rep 41 644 (PDF # 01-087-0976), 1996.
[25] R.D. Shannon, C.T. Prewitt, Acta Crystallogr. A 32 (1976) 751–767.
[26] J.A. Campbell, J.P. Laval, M.T. Fernandez-Diaz, M. Foster, J. Alloys Compds. 111 (2001) 323–324.
[27] J.P. Laval, A. Abaouz, B. Frit, A. Lebail, J. Solid State Chem. 85 (1990) 133–143.
[28] M. Ito, C. Goutaudier, K. Lebbou, Y. Guyot, T. Fukuda, G. Boulon, J. Phys.: Condens. Matter 16 (2004) 1501–1521.
[29] A. Ellens, H. Anders, A. Meijerink, G. Blasse, Phys. Rev. B 55 (1997) 173–186.
[30] L.D. DeLoach, S.A. Payne, L.L. Chase, L.K. Smith, W.L. Kway, W.F. Krupke, IEEE J. Quantum Electron. 29 (1993) 1179–1191.
[31] M.A.R.C. Alencar, G.S. Maciel, C.B. Araujo, Appl. Phys. Lett. 84 (23) (2004) 4753–4755.
[32] M.A. Floress-Gonzalez, G. Ledoux, S. Roux, K. Lebbou, P. Perriat, O. Tillement, J. Solid. Stat. Chem. 178 (2005) 989–997.
[33] R. Bazzi, A. Brenier, P. Perriat, O. Tillement, J. Lumin. 113 (2005) 161–167.
[34] X. Wang, X. Kong, G. Shan, Y. Yu, Y. Sun, L. Feng, K. Chao, S. Lu, Y. Li, J. Phys. Chem. B 108 (2004) 18408–18413.
[35] L. Zhang, H. Hu, J. Phys. Chem. Solid 63 (2002) 575.
[36] P.S. Golding, S.D. Jackson, T.A. King, M. Pollnau, Phys. Rev. B 62 (2000) 856–864.
[37] M. Pollnau, D.R. Gamelin, S.R. Luthi, H.U. Gudel, M.P. Hehlen, Phys. Rev. B 61 (2001) 3337–3346.
[38] J.A. Capobianco, J.C. Boyer, F. Vetrone, A. Speghini, M. Bettinelli, Chem. Mater. 14 (2002) 2915–2921.
[39] A. Patra, C.S. Friend, R. Kapoor, P.N. Prasad, Chem. Mater. 15 (2003) 3650–3655.
[40] F.A. Auzel, IEEE 6 (1993) 758–786.